Micron 163 (2022) 103363

Contents lists available at ScienceDirect

Micron

journal homepage: www.elsevier.com/locate/micron

Short communication

Background subtraction in electron Compton spectroscopy

B.G. Mendis

Dept. of Physics, Durham University, Durham, DH1 3LE, UK

ARTICLE INFO

Keywords:
Compton scattering
Fourier log deconvolution
Multislice
Dynamical scattering

ABSTRACT

Compton scattering in electron energy loss spectroscopy (EELS) is used to quantify the momentum distribution of occupied electronic states in a solid. The Compton signal is a broad feature with a width of several hundred eV. Furthermore, the weak intensity results in a low peak-to-background ratio. Removing the background under the Compton profile is therefore particularly challenging, especially if there is an overlap with EELS core loss edges. Here an empirical background subtraction routine is proposed that uses input data from a bright-field EELS spectrum that does not have a Compton signal. The routine allows for multiple elastic-inelastic scattering within the EELS collection angles. Background subtraction is demonstrated on a Compton profile in silicon that overlaps with the Si L-edge. Systematic errors in the method are also discussed.

1. Introduction

Compton scattering in dark-field electron energy loss spectroscopy (EELS) provides information on the ground state projected momentum density distribution of electronic levels in a solid (Williams et al., 1984; Schattschneider and Exner, 1995; Feng et al., 2013, 2019; Talmantaite et al., 2020; Mendis and Talmantaite, 2022). Due to Fermi-Dirac statistics and the large momenta of solid-state electrons (Kittel, 2005) the Compton peak is broadened over an energy loss range spanning several hundred eV. Furthermore, the weak Compton signal is superimposed on an EELS background that must be accurately subtracted in order to extract reliable electronic structure data. The traditional EELS background subtraction method of extrapolating an analytical function, such as a power law (Egerton, 2011; Fung et al., 2020), however breaks down over the large energy loss range of a Compton profile. Overlap with core loss edges in the EELS spectrum further complicates background removal. An example is shown in Fig. 1a; the Compton profile appears as a weak signal superimposed on a rapidly varying Si L-edge background and has a width greater than 700 eV.

Su et al. (1992) proposed an analytical method, that includes multiple elastic-inelastic scattering, to remove the background. This model however assumed an isotropic solid, and is therefore not valid when the specimen is crystalline and in an orientation that is strongly diffracting. Furthermore, calculating the shape of core loss edges is a non-trivial task (Mizoguchi, 2010, Mendis and Ramasse, 2021), which makes it difficult to remove the background when there is strong overlap between the Compton profile and a core loss edge (e.g. Fig. 1a). Therefore, a more robust background subtraction procedure, which is ideally based on experiment rather than simulation, is desirable. A potential method is schematically illustrated in Figs. 1b and 1c. The Compton profile is acquired in centred dark-field EELS mode, with tilted illumination and with the EELS detector along the electron optic axis (Fig. 1b). On the other hand, a bright-field EELS spectrum (Fig. 1c), acquired from the same region of the sample but with normal beam incidence will not have a Compton signal, since at small scattering angles the Compton energy loss is less than the binding energy of the solid-state electrons (Talmantaite et al., 2020). Therefore, by subtracting a suitably normalised bright-field EELS spectrum from the dark-field EELS spectrum the background under the Compton profile could potentially be removed. However, we have found this approach does not always produce satisfactory results, which is apparent by examining Figs. 1b and 1c more closely. First the distance travelled through the specimen will be different for a tilted and normal incidence beam, which alters the degree of multiple inelastic scattering. Furthermore, the specimen diffraction conditions are also different. Bragg diffraction and thermal diffuse scattering will alter the angular distribution of energy loss electrons. However, only those electrons that exit the specimen in the direction of the EELS spectrometer, i.e. parallel to the electron optic axis in Figs. 1b, 1c, are detected in the far-field. The multiple elastic-inelastic scattering contribution will therefore also be different between the bright-field and dark-field EELS spectra.

In this Short Communication the bright-field EELS background subtraction method is modified to allow for variations in multiple inelastic and elastic-inelastic scattering. The advantage of this new approach is that it is entirely empirical, can be applied to almost any sample and does not require any complex modelling of the background. The theory

---

E-mail address: b.g.mendis@durham.ac.uk.

https://doi.org/10.1016/j.micron.2022.103363
Received 29 July 2022; Received in revised form 26 September 2022; Accepted 27 September 2022

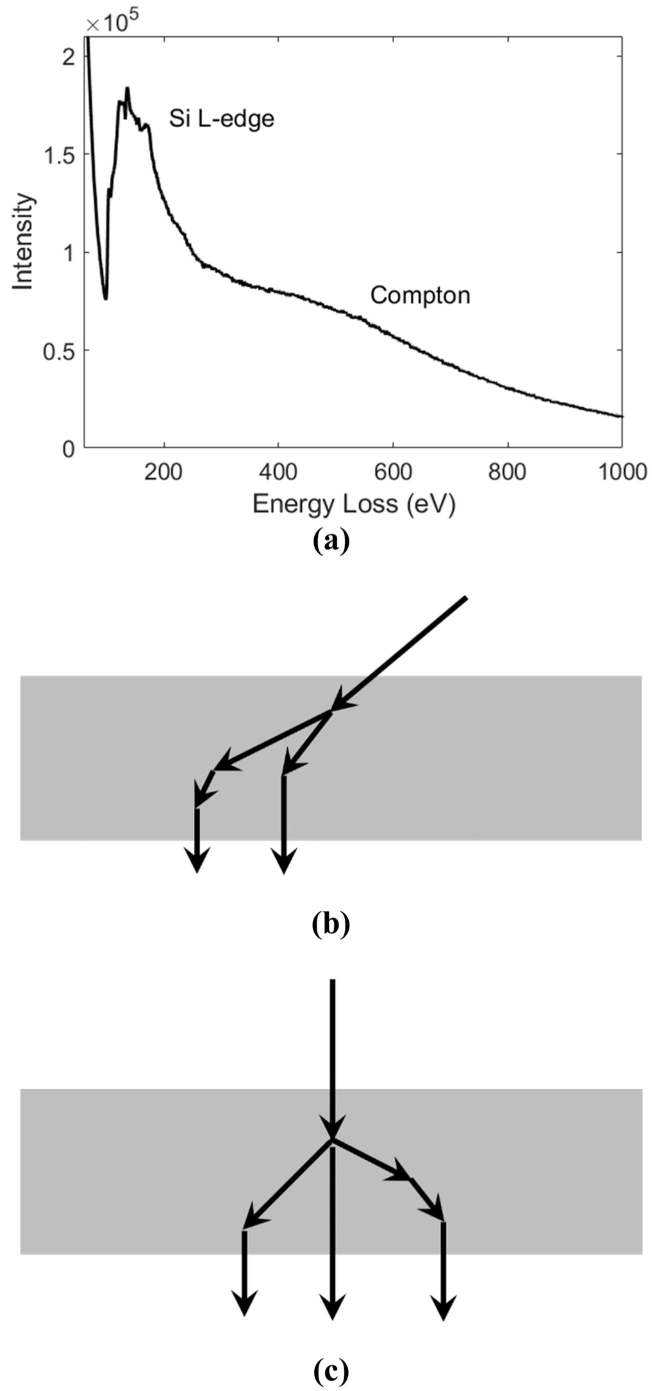

Fig. 1. : (a) Dark-field EELS spectrum from a silicon sample showing the Si L-edge and overlapping Compton profile. (b) and (c) are schematic illustrations of potential electron beam scattering paths within the sample for dark-field and bright-field EELS respectively. The EELS spectrometer is along the electron optic axis in the far-field, so that only electrons that exit the specimen parallel to the optic axis are detected.

is outlined in Section 3. Section 2 describes the experimental procedure, while results are presented in Section 4.

2. Materials and methods

The background subtraction routine is tested on the Compton profile in Fig. 1a, which has previously been reported in Mendis and Talmantaite (2022). This particular example was chosen due to the complexity of the background, which contained the Si L-edge, and therefore poses significant challenges for background subtraction. The EELS spectrum was acquired in centred dark-field image mode from an ion-beam polished, [110]-oriented silicon sample, using a 200 kV JEOL 2100 F field emission gun transmission electron microscope (TEM) and Gatan Tridiem EELS spectrometer. The parallel electron beam was tilted 48.8 mrad away from the [110] zone-axis using the microscope beam tilt coils and was in the 004 Bragg diffraction condition. The EELS spectrometer was along the electron optic axis, and had a 5.3 mrad collection semi-angle, as defined by the objective aperture used for centred dark-field imaging. A bright-field EELS spectrum was also acquired from the thinnest possible region of the specimen in image mode with no objective aperture (the EELS collection semi-angle is therefore only limited by the TEM vacuum tube). The single scattering distribution for this spectrum is extracted via Fourier log deconvolution (Section 3), performed using Gatan Digital Micrograph software assuming a reflected tail model for the zero loss peak. It is important that the specimen is weakly diffracting when acquiring the bright-field EELS spectrum. This condition was satisfied by tilting the specimen 213 mrad away from the [110] zone-axis; the resulting diffraction pattern did not reveal any Bragg reflections that were strongly excited. All EELS spectra were acquired with 0.5 eV/channel dispersion. The low and high energy loss regions were acquired separately, and subsequently spliced to ensure a good signal-to-noise ratio over the entire spectrum.

Multiple elastic-phonon/plasmon scattering was simulated using the multislice method described in Mendis (2019) and Barthel et al. (2020). Here plasmon energy loss events are modelled using Monte Carlo methods within a standard frozen phonon multislice simulation for (pseudo) elastic scattering. Specifically, computer generated random variables are used to estimate the plasmon scattering path length and angles. The plasmon mean free path in silicon is 105 nm and the critical scattering angle is 27.6 mrad (Mendis, 2019). The [110] silicon supercell was 700 Å thick and had lateral dimensions 37.8 Å x 38.2 Å, or equivalently $7a_o$ x $5\sqrt{2}a_o$, where a_o is the unit cell lattice parameter. The incident electron beam was a 200 kV plane wave tilted 48.8 mrad away from the [110] zone-axis and in the Bragg condition for the 004 reflection. The specimen thickness and electron beam match the experimental conditions for the dark-field EELS spectrum in Fig. 1a. Ishizuka's (1982) transmission and propagator functions for tilted illumination are used in the multilsice simulation, with the supercell divided into slices that are $a_o/\sqrt{8}$ or 1.9 Å in thickness. The projected potential for each slice was calculated using Kirkland's (2010) atom scattering factors with 512 $\times$ 512 pixel sampling. A 0.078 Å rms random displacement was imposed on each atom to model thermal diffuse scattering. A total of 3000 frozen phonon configurations were simulated for improved statistics (see also Section 4), the results being classified according to the number of plasmon scattering events.

3. Theory

The starting point is to express the background EELS spectrum $I(E)$ as the sum of multiple inelastic scattering distributions:

$$I(E) = aS(E) + bD(E) + cT(E) + \ldots \tag{1a}$$

$$a + b + c + \ldots = 1 \quad (0 \le a, b, c, \ldots \le 1) \tag{1b}$$

where $S(E), D(E)$ and $T(E)$ are the single, double and triple inelastic scattering distributions which do not contain a Compton signal and a, b and c are the corresponding linear coefficients. $S(E)$ is derived from a bright-field EELS spectrum using Fourier log deconvolution (Egerton, 2011). Higher order inelastic scattering distributions are calculated iteratively, i.e. $D(E) = \alpha S(E) \otimes S(E)$, $T(E) = \beta D(E) \otimes S(E)$ etc., where α, β are normalisation constants and the $\otimes$ symbol represents a convolution operation. The integrated intensities for the dark-field EELS spectrum, $I(E)$ and all inelastic scattering distributions are normalised to unity, which imposes the condition given by Eq. (1b) on the linear coefficients. The energy loss range for intensity normalisation must be chosen so that there is no overlap with the Compton profile.

The linear coefficients a, b, c etc. must be suitably chosen so that $I(E)$ reproduces the pre-Compton background region in the measured dark-field EELS spectrum $O(E)$. This requires minimising the χ^2 metric for Poisson statistics (Hughes and Hase, 2010):

$$\chi^2 = \sum_i \frac{\left[O(E_i) - I(E_i)\right]^2}{I(E_i)} \tag{2}$$

where the summation is over energy loss channels E_i that precede the Compton profile. The inelastic scattered intensity is assumed to be a Poisson distribution (Egerton, 2011):

$$I_n = \frac{1}{n!}\left(\frac{t}{\lambda}\right)^n I_0 \tag{3}$$

where I_n is the intensity of n^{th}-order inelastic scattering, t is the specimen thickness and λ is the inelastic mean free path. The linear coefficients in Eq. (1a) must therefore have fixed values if the background spectrum $I(E)$ were to follow a Poisson distribution. The fact that the linear coefficients are allowed to be 'free' variables, subject to the constraint imposed by Eq. (1b), is because the angular distribution of the energy loss electrons depends on multiple elastic-inelastic scattering. The fraction of I_n passing through the EELS aperture may therefore deviate from a Poisson distribution.

The Fourier log deconvolution routine for extracting $S(E)$ assumes a Poisson distribution for I_n and therefore the EELS collection angle must be as large as possible (Egerton, 2011). Hence the bright-field EELS spectrum is acquired in image mode with no objective aperture (Section 2). Strictly speaking, the large collection angle would mean that there is some contribution from the Compton signal, which could potentially lead to errors in background subtraction. However, the bright-field EELS spectrum is found to be dominated by small angle scattering, and therefore any Compton signal is buried within the experimental noise.

The bright-field EELS spectrum must also be acquired from a thin sample region that is weakly diffracting. This is because the path length of any Bragg diffracted or thermal diffuse scattered electrons through the specimen is longer than the unscattered beam (Fig. 1c), meaning that the thickness t in the Fourier log routine is not well defined. From Eq. (3), the inelastic intensity is linear in thickness for only I_1, so that for accurate results I_2 and other higher order intensity terms must be negligible. Furthermore, it has been shown theoretically that a Poisson intensity distribution is valid when the inelastic scattering is highly delocalised, such as, for example, in plasmon excitation (Mendis, 2020). For more localised interactions, such as core loss edges, channeling of the electron beam can influence the inelastic intensity (Taftø and Krivanek, 1982; Kimoto et al., 2008). Channeling is however suppressed by the kinematical diffraction conditions required for acquiring the bright-field EELS spectrum.

4. Results and discussion

The low and high energy loss regions of the bright-field EELS spectrum are shown in Figs. 2a and 2b respectively. The (t/λ) value for this spectrum is only 0.24, and inevitably there are artefacts due to the specimen free surfaces, such as a surface plasmon peak at ~8.5 eV (Reed et al., 1999) and an O K-edge due to surface oxidation. Nevertheless, these features are minor compared to the bulk features in the EELS spectrum. For example, the dominant energy loss is due to bulk plasmon excitation at 17 eV. Fourier log deconvolution gives the single scattering distribution $S(E)$, from which higher order scattering distributions can

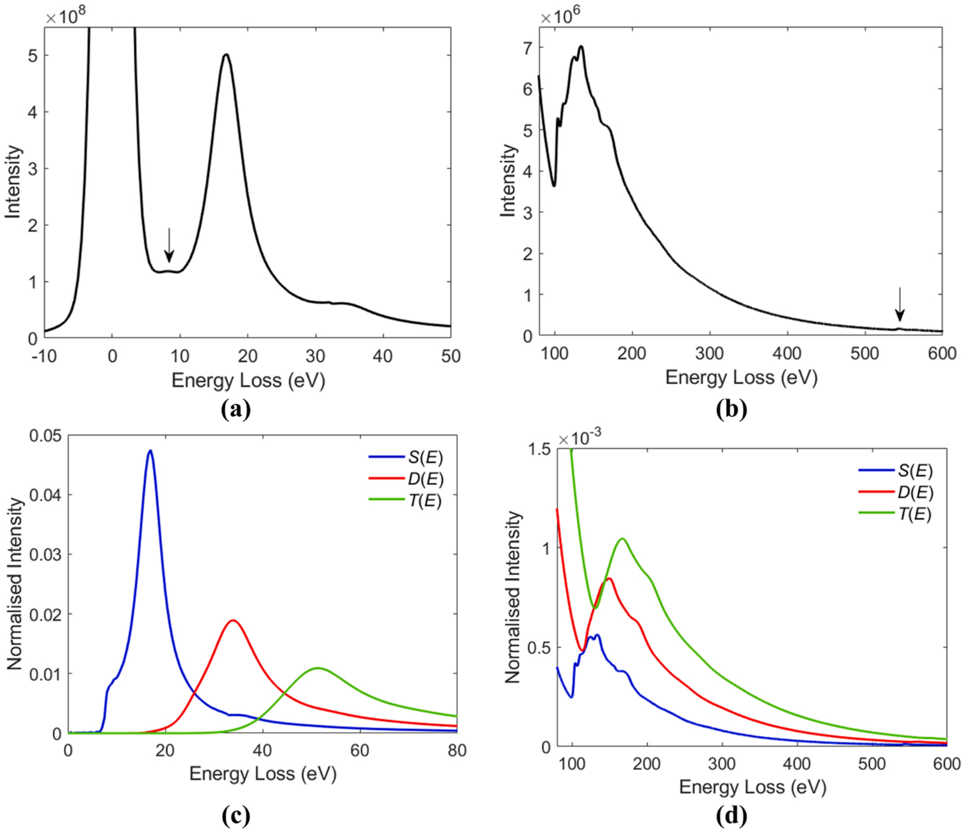

(a) (b) (c) (d)

Fig. 2. : (a) and (b) are the low and high energy loss regions of the bright-field EELS spectrum. The arrows indicate surface plasmons in the low loss region and O K-edge in the high energy loss region. The single $S(E)$, double $D(E)$ and triple $T(E)$ inelastic scattering distributions are superimposed in (c) and (d), which cover the low and high energy loss regions respectively. For each distribution, the integrated intensity within a 0–150 eV energy loss range is normalised.

also be derived. As mentioned in Section 3 for the extracted $S(E)$ to be accurate multiple inelastic scattering must be negligible. For $(t/\lambda) = 0.24$, Eq. (3) predicts that the I_2/I_1 ratio is 12%. On the other hand, least squares fitting Gaussian profiles to the plasmon peaks in the bright-field EELS spectrum results in a much smaller ratio of ~1% for double to single plasmon excitation. Since plasmons have a high scattering cross-section the above plasmon ratio should be approximately I_2/I_1, which is however not the case here. Systematic errors in fitting a simple Gaussian curve to the plasmon peak shape may be a contributing factor to the discrepancy, as well as the presence of some surface plasmon intensity. Nevertheless, it is clear from Fig. 2a that single bulk plasmon excitation, and by extension single bulk inelastic scattering, is by far the dominant process, so that $S(E)$ is assumed to be sufficiently accurate for our purpose. $S(E)$ and other higher order inelastic scattering distributions are shown in Figs. 2c and 2d for the low and high energy loss regions respectively.

A reflected tail model was used to remove the zero loss peak from the dark-field EELS spectrum in Fig. 1a. The pre-Compton background of the resulting spectrum was modelled by least squares fitting multiple scattering distributions derived from the bright-field EELS spectrum (Eqs. 1a-1b). A 10–150 eV energy window was chosen for least squares fitting using scattering distributions up to third order. A comparison of the measured and fitted spectra are shown in Figs. 3a and 3b for the low and high energy loss regions respectively. There is reasonable agreement between the two spectra over the entire pre-Compton energy loss range. The difference spectrum in Fig. 3c represents the background subtracted Compton profile. The Si L-edge onset has been undersubtracted, while the pre-edge background is oversubtracted. The background subtraction errors are largest at the Compton edge onset, since the Compton signal intensity is relatively weak in this region compared to the background. However, at the Compton peak maximum and beyond any background subtraction error will have a smaller effect, as evidenced by the smoother appearance of the difference spectrum (Fig. 3c). The high energy tail of the difference spectrum could therefore be used for a more accurate Compton analysis of the solid. Furthermore, by increasing the Compton scattering angle the Compton peak position can be shifted to higher energy loss (Talmantaite et al., 2020), thereby improving the quality of background subtraction, although due consideration must also be given to the weaker signal at large scattering angles.

Note that the Compton profile shape in Fig. 3c is highly asymmetrical due to strong Bragg diffraction within the sample. A detailed analysis of the Bragg scattering mechanisms and its effect on the above Compton profile can be found in Mendis and Talmantaite (2022). In that paper the Compton profile was simulated using a double multislice technique. The simulated Compton profile is superimposed in Fig. 3c, and shows good agreement with the experimental result, especially around the peak maximum. The agreement is less satisfactory at higher energy loss, which is likely due to inaccuracies in the simulation, as is clear from the kink in the simulated profile at ~625 eV. The overall good agreement between the two profiles further supports the validity of the background subtraction routine proposed here.

The best fit linear coefficients in Fig. 3 are $a = 0.891$, $b = 0.108$ and $c = 0.001$. Since the energy loss range for least squares fitting contained the high intensity plasmon peaks, the linear coefficients must be approximately equal to the multiple plasmon scattering probability over the EELS collection angles. This can be tested via plasmon multislice simulations (Section 2). Figs. 4a-4d show multislice simulated zero, single, double and triple plasmon excitation diffraction patterns respectively. Plasmon scattering broadens the width of the unscattered and Bragg reflections, which is clearly observed in the single plasmon diffraction pattern, but less so for double and triple plasmon excitation due to a lack of convergence, e.g. there were only 14 cases of triple plasmon scattering out of a total of 3000 multislice iterations. The EELS collection aperture used for Compton measurement is superimposed in each diffraction pattern. The integrated intensity within the EELS aperture for single, double and triple plasmon excitation is in the ratio

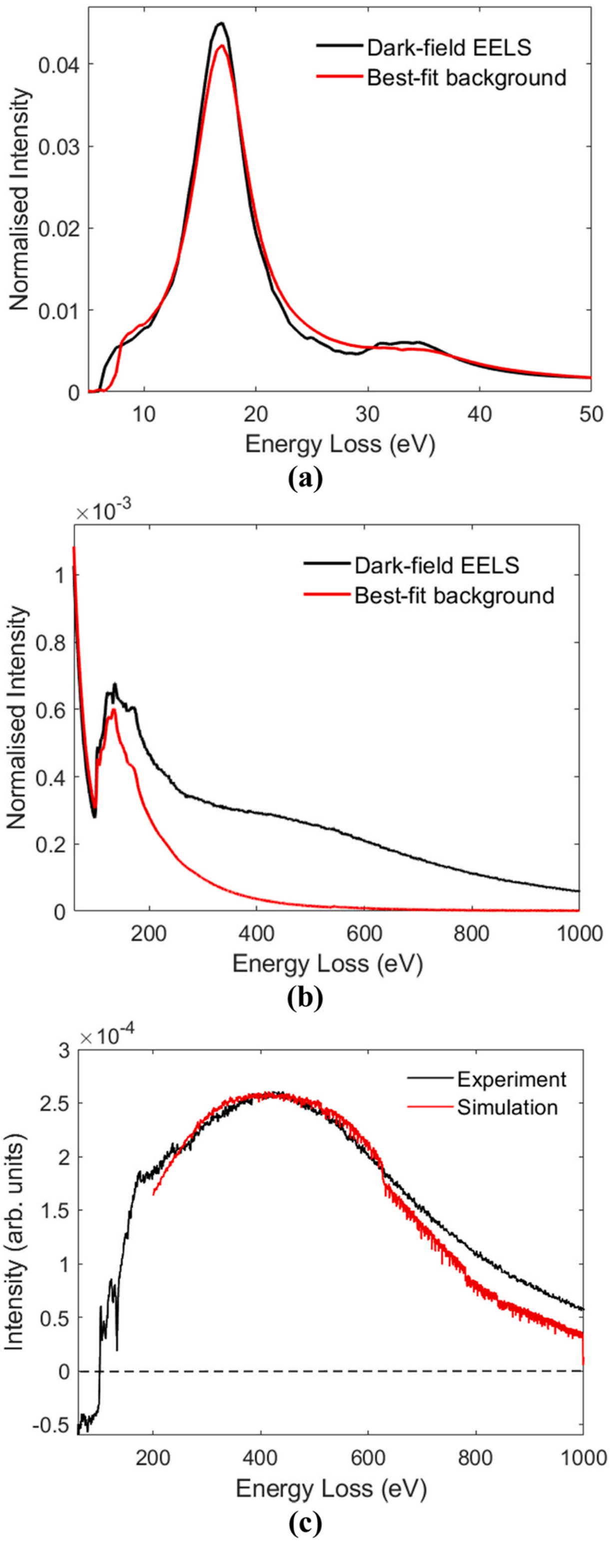

Fig. 3. **:** Inelastic dark-field EELS spectrum and the best fit background. The latter was determined from Eqs. 1a-1b. The integrated intensity within a 10–150 eV energy window of the dark-field EELS spectrum was normalised before fitting. (a) and (b) are the low and high energy loss regions respectively. (c) is the experimental difference spectrum representing the background subtracted Compton profile. The simulated Compton profile from Mendis and Talmantaite (2022) is also superimposed. For direct comparison, the maximum intensity of the simulated profile is adjusted to match experiment.

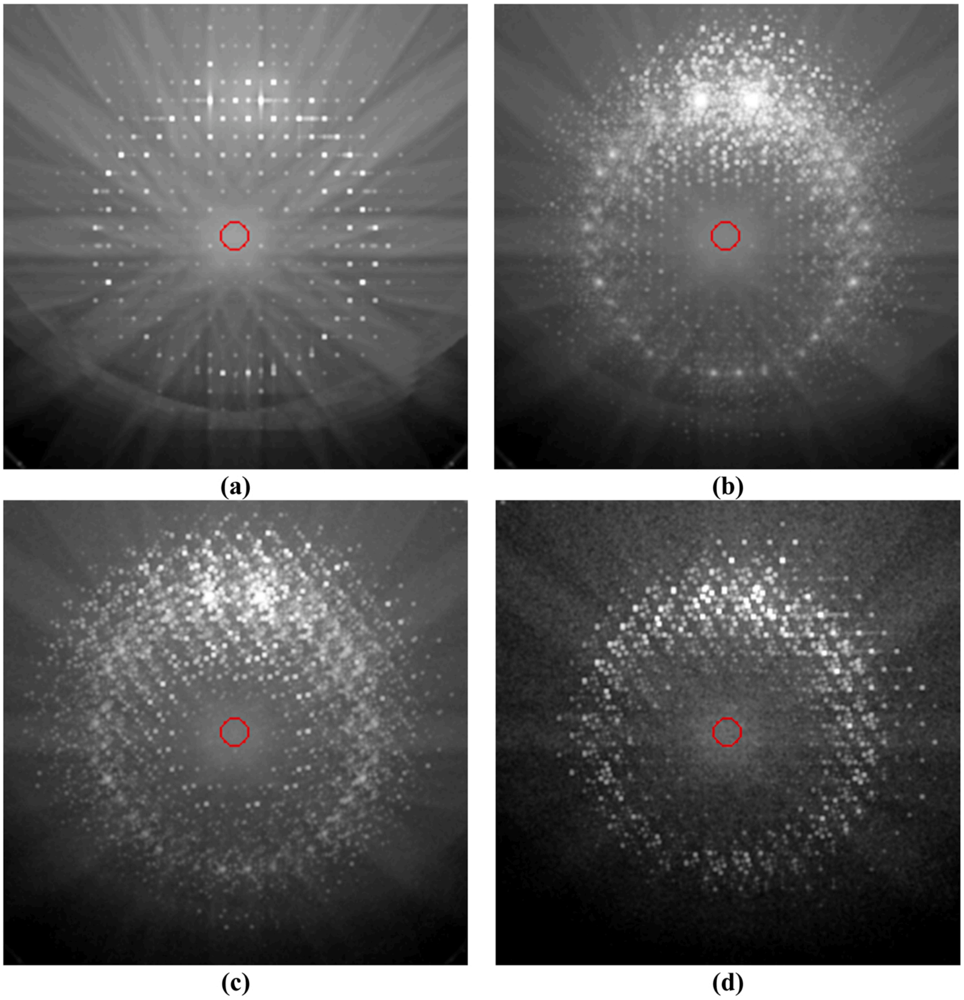

Fig. 4. **:** Multislice simulated (a) zero, (b) single, (c) double and (d) triple plasmon excitation diffraction patterns for dark-field EELS experimental conditions. The intensity is displayed on a logarithmic scale to reveal fine features such as Kikuchi bands. The red circle in each figure outlines the EELS spectrometer aperture.

0.83:0.15:0.02, which is similar to the values obtained from least squares fitting (the error is ± 0.01 based on the convergence of the simulations). This confirms that the best fit linear coefficients represent the relative fraction of multiple inelastic scattering as measured by the EELS spectrometer. The linear coefficients may vary from the global average, due to multiple elastic-inelastic scattering and finite size of the EELS aperture.

Finally, consider the potential sources of error in background subtraction. The conflicting requirement of using a thin specimen region for acquiring the bright-field EELS spectrum without introducing any free surface artefacts has already been highlighted. The single scattering distribution $S(E)$ extracted from Fourier log deconvolution has the same energy resolution as the bright-field EELS spectrum (Egerton, 2011). However, the longer acquisition time for Compton measurements may mean the effective energy resolution for dark-field EELS is degraded by instabilities in the EELS spectrometer and/or room environment. In principle, this can be mitigated by convolving $S(E)$ with a Gaussian. However, the quality of plasmon (Fig. 3a) and pre-Si L edge background (Fig. 3b) fitting suggests that there is no significant difference in energy resolution for this particular case. There are nevertheless some fundamental errors in Eq. (1a) as a potential background fitting model. The first is that dispersion is not taken into account. For example, the plasmon energy increases with scattering vector magnitude and above a critical wavenumber is damped by single electron excitations (Watanabe, 1956). Furthermore, for anisotropic materials such as graphite and boron nitride there is a change in the core loss edge shape with scattering vector (Leapman et al., 1983). Dispersion and anisotropy are averaged over a large angular range in $S(E)$, but can be important for the limited collection angles in a dark-field EELS spectrum. Second Eq. (1a) treats different inelastic scattering mechanisms on an equal footing. As an example, for double scattering both double plasmon excitation and the (Si L-edge + single plasmon) excitation have the same linear coefficient. The former affects the background under the Si L-edge, while the latter alters the Si L-edge shape. The cross-section for both plasmon and core loss scattering have a Lorentzian distribution with a characteristic scattering angle given by $\theta_E = (E/2E_o)$, where E is the energy loss and E_o is the primary beam energy (Egerton, 2011). For silicon, θ_E for the Si L-edge is larger by a factor of ~6 compared to plasmons. Strictly speaking, the two scattering events should therefore have different weightings, rather than a single linear coefficient assigned to the double scattering distribution $D(E)$. However, it is unlikely this would lead to a significant error in the present example, since the 5.3 mrad EELS collection semi-angle is significantly larger than θ_E, which has a calculated value of 0.25 mrad for the Si L-edge and 0.04 mrad for plasmons.

5. Summary

A background subtraction routine for electron Compton spectroscopy is presented, which accounts for multiple elastic-inelastic scattering within the angular range for EELS detection. The background is modelled using multiple inelastic scattering distributions derived from a bright-field EELS spectrum, which has the Compton signal suppressed.

Unlike the previous method of Su et al. (1992) this new background subtraction procedure is largely empirical and does not require any complicated simulations. Application to a Compton profile in silicon that shows strong overlap with the Si L-edge produced satisfactory results, apart from the Compton profile onset region, where the peak-to-background ratio is small. Systematic errors in the background subtraction are also discussed.

Declaration of Competing Interest

The author declares that he has no known competing financial interests or personal relationships that could have appeared to influence the work reported in this paper.

Data Availability

Data will be made available on request.

References

Barthel, J., Cattaneo, M., Mendis, B.G., Findlay, S.D., Allen, L.J., 2020. Angular dependence of fast-electron scattering from materials. Phys. Rev. B 101, 184109.

Egerton, R.F., 2011. Electron Energy-loss Spectroscopy in the Electron Microscope, third ed. Springer, New York.

Feng, Z., Löffler, S., Eder, F., Su, D., Meyer, J.C., Schattschneider, P., 2013. Combined study of the ground and unoccupied electronic states of graphite by electron energy-loss spectroscopy. J. Appl. Phys. 114, 183716.

Feng, Z., Zhang, X., Sakurai, Y., Wang, Z., Li, H., Hu, H., 2019. Compton profile of few-layer graphene investigated by electron energy-loss spectroscopy. Nat. Sci. Rep. 9, 17313.

Fung, K.L.Y., Fay, M.W., Collins, S.M., Kepaptsoglou, D.M., Skowron, S.T., Ramasse, Q. M., Khlobystov, A.N., 2020. Accurate EELS background subtraction- an adaptable method in MATLAB. Ultramicroscopy 217, 113052.

Hughes, I.G., Hase, T.P.A., 2010. Measurements and their Uncertainties. Oxford University Press, Oxford.

Ishizuka, K., 1982. Multislice formula for inclined illumination. Acta Cryst. A 38, 773–779.

Kimoto, K., Ishizuka, K., Matsui, Y., 2008. Decisive factors for realizing atomic-column resolution using STEM and EELS. Micron 39, 257–262.

Kirkland, E.J., 2010. Advanced Computing in Electron Microscopy, second ed. Springer, New York.

Kittel, C., 2005. Introduction to Solid State Physics, eighth ed. John Wiley and Sons, USA.

Leapman, R.D., Fejes, P.L., Silcox, J., 1983. Orientation dependence of core edges from anisotropic materials determined by inelastic scattering of fast electrons. Phys. Rev. B 28, 2361–2373.

Mendis, B.G., 2019. An inelastic multislice simulation method incorporating plasmon energy losses. Ultramicroscopy 206, 112816.

Mendis, B.G., 2020. Theory underpinning multislice simulations with plasmon energy losses. Microscopy 69, 173–175.

Mendis, B.G., Ramasse, Q.M., 2021. Removal of core hole distortion from ionization edges in electron energy loss spectroscopy. Phys. Rev. B 103, 205102.

Mendis, B.G., Talmantaite, A., 2022. Towards electron energy loss Compton spectra free from dynamical diffraction artefacts. Microsc. Microanal. https://doi.org/10.1017/S1431927622012223.

Mizoguchi, T., Olovsson, W., Ikeno, H., Tanaka, I., 2010. Theoretical ELNES using one-particle and multi-particle calculations. Micron 41, 695–709.

Reed, B.W., Chen, J.M., MacDonald, M.C., Silcox, J., Bertsch, G.F., 1999. Fabrication and STEM/EELS measurements of nanometer-scale silicon tips and filaments. Phys. Rev. B 60, 5641–5652.

Schattschneider, P., Exner, A., 1995. Progress in electron Compton scattering. Ultramicroscopy 59, 241–253.

Su, D.S., Jonas, P., Schattschneider, P., 1992. The multiple-scattering problem in electron Compton scattering on solids. Philos. Mag. B 66, 405–418.

Taftø, J., Krivanek, O.L., 1982. Site-specific valence determination by electron energy-loss spectroscopy. Phys. Rev. Lett. 48, 560–563.

Talmantaite, A., Hunt, M.R.C., Mendis, B.G., 2020. Electron Compton scattering and the measurement of electron momentum distribution in solids. J. Microsc. 279, 185–188.

Watanabe, H., 1956. Experimental evidence for the collective nature of the characteristic energy loss of electrons in solids- studies on the dispersion relation of plasma frequency. J. Phys. Soc. Jpn. 11, 112–119.

Williams, B.G., Sparrow, T.G., Egerton, R.F., 1984. Electron Compton scattering of solids. Proc. R. Soc. Lond. A 393, 409–422.